

Proceedings of Meetings on Acoustics

SEPTEMBER 18 2020

New target detection algorithms for volumetric synthetic aperture sonar data

David P. Williams  ; Daniel C. Brown



Proc. Mtgs. Acoust. 40, 070002 (2020)

<https://doi.org/10.1121/2.0001296>



View
Online



Export
Citation



The banner features the ASA logo (a stylized 'A' composed of dots) on the left, followed by the text "ASA" and "LEARN MORE" in a blue button on the right. Below this, the text "Advance your science and career as a member of the **Acoustical Society of America**" is displayed in white and blue on a dark background with abstract circular patterns.



International Conference on Underwater Acoustics

9 September 2020

ICUA 2020: Session 5B

New target detection algorithms for volumetric synthetic aperture sonar data

David P. Williams

Department of Research, Centre for Maritime Research and Experimentation, La Spezia, SP, 19126, ITALY; daniel.williams@cmre.nato.int

Daniel C. Brown

Applied Research Laboratory, Pennsylvania State University, State College, PA, USA; dcbl9@arl.psu.edu

A fast algorithm for the automated detection of buried and proud objects in three-dimensional (3-d) *volumetric* synthetic aperture sonar (SAS) imagery is proposed. The method establishes the positions of underwater targets by finding localized volumes of strong acoustic returns on or within the sediment. The algorithm relies on an important data-normalization step that is grounded in principled physics-based arguments, and it greatly reduces the amount of data that must be passed to a follow-on classification stage. The promise of the approach is demonstrated for man-made objects present in real, measured SAS data cubes collected at multiple aquatic sites by an experimental volumetric sonar system.

1. INTRODUCTION

An unfortunate legacy of former military activities is the contamination of aquatic environments with unexploded ordnance (UXO). In shallow water, proud and buried munitions pose a particular threat to both humans and the environment, so remediation is necessary. To address this pressing issue, several low-frequency sonar systems – importantly, on mobile platforms – have recently been developed.^{1–3} These downward-looking synthetic aperture sonar (SAS) systems, designed to achieve sediment penetration, provide high-resolution three-dimensional (3-d) *volumetric* imagery below the seafloor, making large-scale buried object detection newly feasible. (Other *side-looking* low-frequency sonars^{4,5} generate only 2-d imagery.)

With the introduction of this new sensor modality, there is now a need for automated detection algorithms that can efficiently process enormous 3-d images to rapidly flag suspicious objects for closer inspection during remediation efforts. Relying on humans to visually assess these new data products is both inherently challenging and inefficient. In this work, we propose a novel detection method and demonstrate its promise on real, measured sonar data collected by a newly developed sonar system that is operationally capable. The approach is general in the sense that it can be employed for wide classes of objects of interest, but here it is presented in the context of underwater UXO.

The detection of objects of interest in 3-d data cubes is a goal shared across diverse disciplines. For example, previous work with tomographic medical imaging scans,^{6,7} video scenes possessing a temporal component,^{8,9} hyperspectral data comprising multiple frequency bands,^{10,11} and ground-penetrating radar for buried objects on land^{12,13} all exploit 3-d data cubes that can be mined for valuable information.

But the particularities of *sonar* sensors and the unique challenges of the underwater environment warrant a new approach specially tailored to the physics involved. As such, the main contribution of this work is the development of a data normalization and object detection algorithm for volumetric SAS imagery. These algorithms fill a current capability gap, thereby advancing the feasibility of employing this new class of sensors in real-world UXO remediation operations.

The principal detection algorithm used for volumetric sonar imagery in the literature¹ simply sums the energy at each voxel over multiple pings and compares this quantity to a threshold. A second detection approach¹⁴ for the same system compares moments of the voxel intensities to the local background. But neither approach addresses the complications associated with *near-normal incidence* returns from a strictly downward-looking system.

The remainder of this paper is organized as follows. Sec. 2 describes the proposed algorithms for volumetric SAS imagery, while Sec. 3 presents results of the method on real, measured data for buried and proud man-made targets. Concluding remarks are made in Sec. 4.

2. OBJECT DETECTION ALGORITHM

A. DATA NORMALIZATION

Acoustic waves scatter upon encountering a boundary between two media characterized by a mismatch in acoustic impedance and the roughness of the boundary.¹⁵ The strength of the reflection is determined by the material properties – primarily density and sound speed – of the two media. As a result, the water-sediment interface (*i.e.*, the seafloor) will *not* necessarily produce the strongest backscattered return. For example, in the case of a mud seafloor above a sand substrate, the scattering from the water-mud interface is likely to be lower than the scattering from the deeper mud-sand transition within the sediment itself. But inevitably, there will exist some depth layer that dominates all others, and this necessitates a data normalization pre-processing step.

Suppose there is a raw 3-d data cube of beamformed sonar returns, \mathbf{A} , in a coordinate system (x, y, z)

defined by the cross-track direction x , along-track direction y , and depth from the sonar platform, z . The normalization procedure proposed for volumetric sonar data is as follows:

1. Determine the plane of the interface in the image volume for which returns dominate. Define z' to be the normal to this plane, with $\hat{\theta}$ the angle between z and z' in the y - z plane.
2. Determine and remove the sub-volume, \mathbf{V}_M , of the data cube contaminated by multipath interference associated with the dominant interface.
3. For a given cross-track position x , consider the y - z plane, $\mathbf{A}_x(y, z)$. Compute the median value, $\mu_x(d)$, of pixels located a given distance d from the dominant interface, and divide those pixel values by $\mu_x(d)$. Repeat for each d and x .
4. For a given along-track position y , consider the x - z plane, $\mathbf{A}_y(x, z)$. Compute the median value, $\mu_y(d)$, of pixels located a given distance d from the dominant interface, and divide those pixel values by $\mu_y(d)$. Repeat for each d and y .
5. Convert the normalized data cube to a logarithmic (decibel) scale and truncate the voxel values to a dynamic range of $[0, 40]$.

Space constraints prevent us from detailing the procedure more formally, but we shall provide insight into the algorithmic choices made. An implicit assumption in the normalization procedure is that any given sediment layer in the imaged volume is approximately uniform in depth, with this justified by the nature of underwater sediment transport processes and diagenesis.¹⁶ We also assume that any bathymetric variation of the dominant interface plane occurs only in the (much longer) along-track direction. That is, the depth of the dominant interface at a given along-track position is taken to be constant. This is reasonable given the relatively narrow sonar swath in the cross-track direction, coupled with the fact that relief changes typically manifest only over longer spatial scales. This simplifies step 1 to determining a single angle $\hat{\theta}$ in the y - z plane characterizing the slope of the dominant interface. In practice this is achieved by applying a Radon transform on the 2-d image slice at the i th cross-track position to determine θ_i , and then taking $\hat{\theta}$ to be the mode of the set comprising all θ_i .

In very shallow water, the presence of multipath scattering resulting from multiple reflections – *i.e.*, from the sonar transmitter down to the dominant sediment interface, up to the water-air interface, back to the dominant sediment interface, and back to the sonar receiver – can contaminate the data cube.¹⁷ With $m_z = \tan \hat{\theta}$ the slope of the dominant sediment interface, simple geometry dictates that a multipath replica of that interface will manifest with a slope of $2m_z$.¹⁸ With knowledge of the absolute depth of the water column (*i.e.*, from the air-water interface), one can then determine the region of the data cube where multipath interference will occur via the corresponding equations of the lines (or planes) associated with $2m_z$. The data in the identified multipath-contaminated region is discarded because any authentic signal in the data cube's multipath region will be overwhelmed by the multipath return of the dominant interface.

In steps 3 and 4, cross-track positions are considered before along-track positions in order to first remove the known scattering dependence on grazing angle¹⁹ (and hence cross-track position). The end result is a data cube in which the background is approximately uniform regardless of depth.

B. OBJECT DETECTION

The object detection task we concern ourselves with is a classic remote-sensing problem of locating a target signal amid a noisy background.²⁰ Common to this class of problems is the need to set two parameters that are tied to the target of interest: a window related to the size of the target, and a threshold related to the relative strength of the target.

In the 1-d case, a simple solution involves estimating the background level and assuming that signals above some threshold indicate a potential target signal. Here we deal with 3-d imagery, but the underlying

principles are unchanged. Our proposed algorithm computes a local estimate of the background intensity around each voxel, which are the potential target signals. If the target-to-background ratio exceeds the threshold, the voxel is flagged. And if a connected volume (*i.e.*, “blob”) of such flagged voxels exceeds the minimum size of objects of interest, a discrete alarm is generated.

The approach taken in this work is motivated by the UXO application in which the size and shape of objects of interest can vary considerably, from individual bullets or fragments to larger intact shells and munitions. As such, we desire a general purpose detector that is not tied to one specific object, but rather can detect a wide class of objects. Our approach largely extends the Mondrian detector²¹ to 3-d imagery. But given the 3-d geometry of the problem, there will be no acoustic shadow clues (as are present in 2-d side-looking sonar images^{22,23}) to exploit. Instead the only insight to leverage is that the man-made objects of interest are assumed to be acoustically harder, producing stronger returns, than the surrounding sediment.

The normalization process applied to the data permits the use of a single threshold for the entire 3-d data cube. In addition, the necessary signal and background estimates can be performed extremely efficiently using integral images.²⁴

Let \mathbf{A} be a data cube in which targets are to be detected. The integral image \mathbf{W} of \mathbf{A} represents the summed volume of intensities defined by

$$W(x, y, z) = \sum_{x' \leq x} \sum_{y' \leq y} \sum_{z' \leq z} A(x', y', z'). \quad (1)$$

The summed intensity over any rectangular volume with corners specified by α^j for $j \in \{0, 1\}^3$ can then be readily computed as

$$U = \sum_{j \in \{0, 1\}^3} (-1)^{3 - \|j\|_1} W(\alpha^j), \quad (2)$$

where $W(\alpha)$ is the integral image at voxel α . Thus, given specified rectangular volumes to be used for the target (“signal”) and background (“noise”) estimation, the mean intensity of each quantity centered at each voxel in the data cube can be computed quickly.

To ensure that potential target voxels are excluded from the background volume calculations, a third rectangular volume is employed to act as a “guard” window (*à la* a split window). The target (**T**), guard (**G**), and background (**B**) volumes are concentric, increasing in size. In this work, the sizes (in units of m) of the rectangular volumes are set to

$$\gamma(x, y, z) = [0.12, 0.12, 0.06] \quad (3)$$

$$\mathbf{T} = \gamma \quad (4)$$

$$\mathbf{G} = 4\gamma \quad (5)$$

$$\mathbf{B} = 6\gamma, \quad (6)$$

with the parameters reflecting the sizes of objects of interest.

Let $T(x, y, z)$, $G(x, y, z)$, and $B(x, y, z)$ represent the summed intensity of the target, guard, and background volumes centered at voxel (x, y, z) , respectively. A binary data cube map is then constructed based on the result of the test

$$\left(\frac{n_B - n_G}{n_T} \right) \left(\frac{T(x, y, z)}{B(x, y, z) - G(x, y, z)} \right) \geq \tau_s, \quad (7)$$

where τ_s is related to the minimum (relative) intensity of objects of interest, and $n.$ indicates the number of voxels used in a given sum (to effect mean values). Each connected volume in this map that exceeds τ_v , the minimum volume of objects of interest, is then converted to a discrete alarm.

When using integral images, it should be noted that the voxel values must be non-negative. Additionally, it is imperative that sufficient numerical precision is maintained,²⁵ an issue that is likely to be especially

germane when dealing with large data cubes. A simple way to verify that no overflow errors have manifested is to exploit the inversion formula

$$\tilde{A}(x, y, z) = \sum_{j \in \{0,1\}^3} (-1)^{2 - \|j\|_1} W(\alpha^j), \quad (8)$$

and confirm that the result, $\tilde{\mathbf{A}}$, matches the original data cube \mathbf{A} exactly. In this work, 64-bit precision was required to avoid undesired arithmetic overflow.

C. FEATURE EXTRACTION

Volumetric data cubes from sonar surveys can be enormous products, but the vast majority of the content is likely to be benign and irrelevant for the UXO remediation problem. At the same time, human visualization of an entire 3-d data cube is not trivial, and techniques that rely on basic data slices or projections invariably discard considerable information. Therefore, a major role of the detector is to rapidly decrease the amount of data that must be examined further. Indeed, the contacts flagged in the detection stage are expected to be passed on to a more sophisticated classification stage.

But additional processing or data-collection surveys may also be undertaken based on the results of the detection stage. For example, fully-complex 3-d beamforming, a very computationally demanding procedure, can be performed over limited volumes centered on contact locations, with this enabling the generation of acoustic color plots²⁶ that can reveal informative aspect and frequency-dependent responses associated with the object. Alternatively, additional physical surveys at sea can be undertaken to collect more comprehensive data on detected contacts, such as at new aspects or with different sonar settings (*e.g.*, grazing angle, waveform, depth). For these reasons, it can be valuable to provide an *ordered* list of contacts to prioritize subsequent operations.

To that end, we extract a pair of primitive features that can be combined into an overall detection “score.” Specifically, a size feature, f_1 , that is the volume of a contact’s voxels that exceeded the threshold τ_s is computed. A strength feature, f_2 , that is the mean of the contact’s $n = 64$ largest voxel values is also computed. The final detection score by which the contacts can be ordered is taken to be the geometric mean of these two features,

$$f = \sqrt{f_1 f_2}, \quad (9)$$

as this effectively provides an approximation to the contact’s overall intensity (and for the UXO problem, explosive potential or threat).

Other basic shape and orientation features can also be extracted, but we abstain from doing so given that the future classification stage is envisioned to employ convolutional neural networks (CNNs),²⁷ for which explicit features are unnecessary.

3. EXPERIMENTAL RESULTS

A. VOLUMETRIC SONAR DATA

The Sediment Volume Search Sonar (SVSS)² is a recently developed low-frequency sonar system designed to address the UXO remediation problem in shallow water environments (*i.e.*, depths less than 5 m). The experimental system features multiple transmitters and a 2-d receiver array that collectively enable the production of 3-d SAS imagery to facilitate the detection of proud and buried objects. The frequency band of operation is approximately 20-35 kHz. A time-domain back-projection beamformer²⁸ is used to transform the raw sonar time series returns into 3-d volumetric imagery comprising voxels that span 2 cm in each dimension.

The challenge of visualizing a 3-d data cube often leads to the use of a 2-d maximum intensity projection (MIP), which collapses the imagery along one of its principal axes by retaining the highest intensity voxels

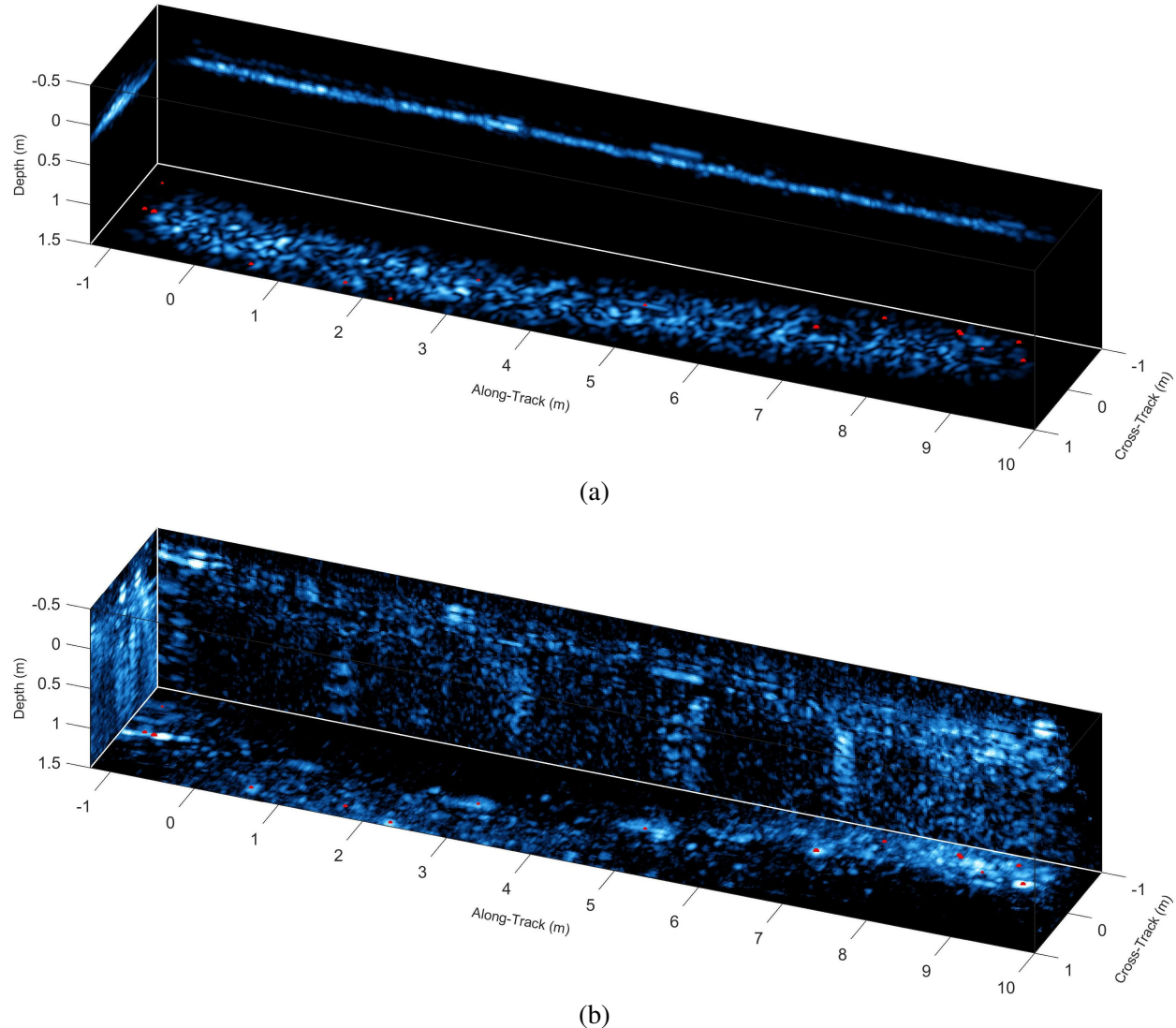


Figure 1: An example SVSS volumetric scene image, from site A, displayed as a trio of MIPs, when (a) the data is raw or (b) normalized. Algorithm detections are marked on the depth MIPs with red dots.

along that axis.²⁹ A typical data cube from the SVSS system, before and after the proposed normalization algorithm described in Sec. 2.1 is shown in Fig. 1 as a set of three 2-d MIPs in a common reference frame. In Fig. 1(a), the dominant interface return obscures target signatures, whereas in Fig. 1(b) it can be observed that the normalization procedure amplifies the signals of interest, including elastic target returns. Localized alarm data cubes (displayed as MIPs) extracted from Fig. 1 of four targets are shown in Fig. 2, along with corresponding object photographs taken during installation. (The 3-d alarm data cubes like in Fig. 2(a)-(d) are what would be the inputs to a subsequent CNN.)

For the results reported in this work, the SVSS system was used to collect data at three sites in the United States, two distinct locations in the Fosters Joseph Sayers Reservoir in Pennsylvania and one location at the Aberdeen Test Center in Maryland. At the Sayers sites, there existed an upper layer of approximately 8 cm of silt atop a clay base; site “A” had a 1.3 m water depth, while site “B” had a 3.0 m water depth. The Aberdeen location, site “C,” featured a sloping sediment of sand, resulting in a water depth that ranged from 1.0 m to 2.5 m. The shallow water meant multipath interference was not insignificant.

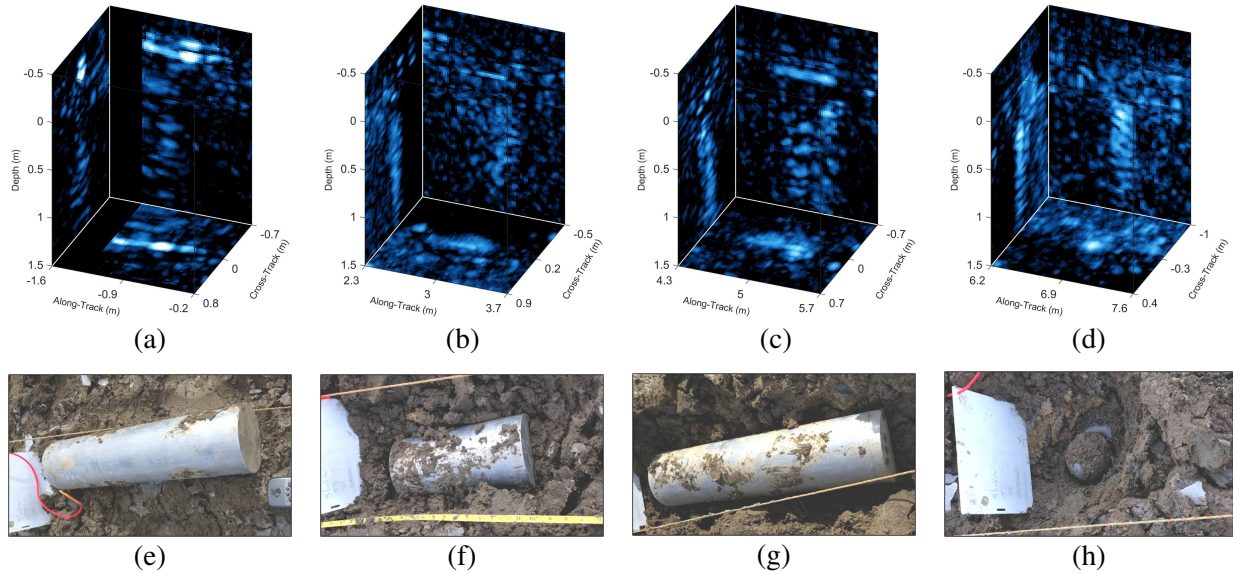


Figure 2: (a)-(d) SVSS alarm cubes (each displayed as a trio of MIPs) of four targets extracted from Fig. 1, and (e)-(h) photographs of the objects during installation (pre-burial). The objects, along with the human-assessments of the sonar imagery in parentheses, are: (a) 4:1 solid aluminum cylinder proud (Large/Strong), (b) 2:1 solid aluminum cylinder buried 5 cm (Large/Weak), (c) 4:1 solid aluminum cylinder buried 3 cm (Large/Strong), (d) 10.2 cm diameter steel shot put buried 19 cm (Small/Strong); the cylinders have 15.2 cm diameters.

The sites were reservoirs that could be drained to facilitate target emplacement. So prior to data collection, various man-made objects were deployed, including aluminum cylinders, steel pipes, steel shot puts, concrete blocks, and an assortment of munitions with diameters ranging from 20 mm to 155 mm. Some objects were placed proud on the sediment, while others were buried to various depths (up to 60 cm) below the water-sediment interface. Data collections at Sayers took place in 2019 at the following times (nominally labeled “1” through “4,” respectively): June, August, early November, and late November. The Aberdeen collection (labeled “5”) occurred in March 2020.

B. RESULTS

The complex physics at play underwater and in the subsediment volume suggest that the collected 3-d data might not always support target detection, regardless of the algorithm employed. Factors such as sediment attenuation, interface scattering levels, the presence of gas bubbles in the sediment, and the relationship between sensor resolution and target dimensions mean that the upper limit on detection capability will likely be less than unity. To assess this possibility, the data from each target opportunity was first visually examined and rated in terms of anomaly size (large or small) and strength (strong or weak) in the imagery. Anomalies that were deemed both small and weak represent a “gray zone” in which detection may or may not actually be feasible.

With these human assessments as a backdrop, the performance of the proposed target detection algorithm at eight distinct data collections, delineated by location and time, are shown in Fig. 3 for proud and buried targets. As can be seen from the figure, performance varies considerably across location (*cf.* collection letters), but also across time (*cf.* collection numbers), the latter variation suggesting strong environmental dependence (*e.g.*, water temperature, microbial activity). However, in all cases, the automated detection performance comported with the expected range based on visual inspection of the imagery.

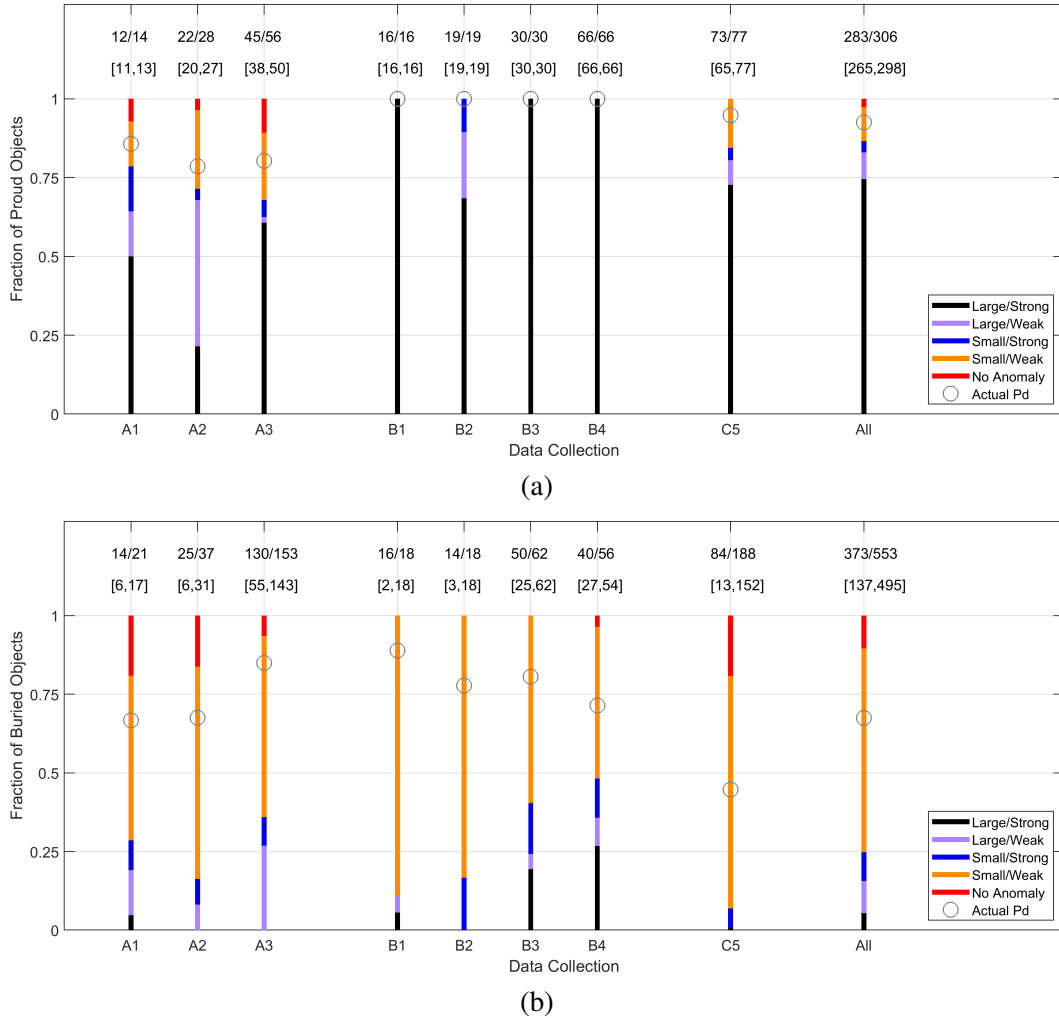


Figure 3: Performance of the detection algorithm for each data collection for (a) proud man-made targets and (b) buried man-made targets, along with the distribution of visual human assessment ratings. Above each bar are the numbers of targets detected vice opportunities, and in brackets the range of targets deemed detectable based on visual human assessment.

The combined detection performance from pooling the proud and buried targets, and using the score from (9), of the various data collections is shown in Fig. 4. Performance is displayed in terms of receiver operating characteristic-like (ROC-like) curves, where the probability of false alarm is replaced by false alarm rate (per unit volume).

4. CONCLUSION

A new detector with 3-d localization ability was designed to rapidly decrease the amount of volumetric SAS data that must be examined further. Algorithm choices were driven largely by the particular physics involved in the problem. The promise of the approach in the context of a new sensor was demonstrated, and fundamental limits on performance based on unavoidable factors were also discussed. Ongoing and future work will see the development of a dedicated CNN-based classification stage in order to reduce the false alarm rate to more acceptable levels.

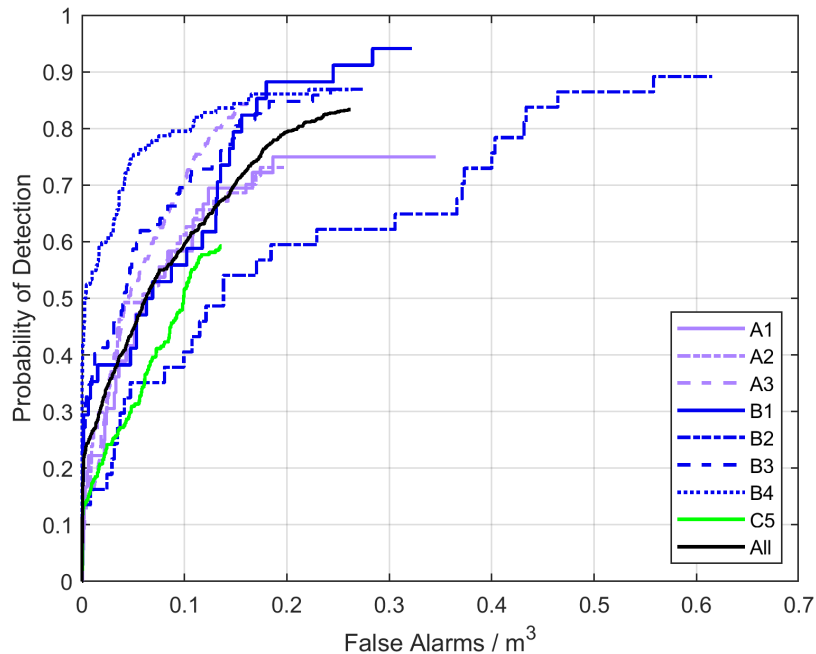


Figure 4: Overall performance of the detection algorithm for each data collection.

ACKNOWLEDGMENTS

This research was supported by the U.S. Department of Defense, through the Strategic Environmental Research and Development Program (SERDP), under Projects MR18-1444 (DPW) and MR-2545 (DCB) in the Munitions Response area. With respect to the latter project, this material is based upon work supported by the Humphreys Engineer Center Support Activity under Contract No. W912HQ-16-C-0006.

REFERENCES

- ¹ S. Schock, A. Tellier, J. Wulf, J. Sara, and M. Ericksen, “Buried object scanning sonar,” *IEEE Journal of Oceanic Engineering*, vol. 26, no. 4, pp. 677–689, 2001.
- ² D. Brown, S. Johnson, I. Gerg, and C. Brownstead, “Simulation and testing results for a sub-bottom imaging sonar,” in *Proceedings of Meetings on Acoustics*, vol. 36, no. 1. Acoustical Society of America, 2019, pp. 1–12.
- ³ T. Marston, D. Plotnick, and K. Williams, “Three dimensional fast factorized back projection for sub-sediment imaging sonars,” in *Proceedings of IEEE OCEANS*, 2019, pp. 1–6.
- ⁴ D. Brown, D. Cook, and J. Fernandez, “Results from a small synthetic aperture sonar,” in *Proceedings of IEEE OCEANS*, 2006, pp. 1–6.
- ⁵ A. Hunter and R. van Vossen, “Sonar target enhancement by shrinkage of incoherent wavelet coefficients,” *The Journal of the Acoustical Society of America*, vol. 135, no. 1, pp. 262–268, 2014.
- ⁶ J. Staal, B. van Ginneken, and M. Viergever, “Automatic rib segmentation and labeling in computed tomography scans using a general framework for detection, recognition and segmentation of objects in volumetric data,” *Medical Image Analysis*, vol. 11, no. 1, pp. 35–46, 2007.

-
- ⁷ B. van Ginneken, A. Setio, C. Jacobs, and F. Ciompi, “Off-the-shelf convolutional neural network features for pulmonary nodule detection in computed tomography scans,” in *IEEE 12th International Symposium on Biomedical Imaging (ISBI)*, 2015, pp. 286–289.
- ⁸ S. Nadimi and B. Bhanu, “Physical models for moving shadow and object detection in video,” *IEEE Transactions on Pattern Analysis and Machine Intelligence*, vol. 26, no. 8, pp. 1079–1087, 2004.
- ⁹ K. Kang, W. Ouyang, H. Li, and X. Wang, “Object detection from video tubelets with convolutional neural networks,” in *Proceedings of the IEEE Conference on Computer Vision and Pattern Recognition*, 2016, pp. 817–825.
- ¹⁰ C. Chang, *Hyperspectral Imaging: Techniques for Spectral Detection and Classification*. Springer Science & Business Media, 2003, vol. 1.
- ¹¹ S. Bourennane, C. Fossati, and A. Cailly, “Improvement of target-detection algorithms based on adaptive three-dimensional filtering,” *IEEE Transactions on Geoscience and Remote Sensing*, vol. 49, no. 4, pp. 1383–1395, 2010.
- ¹² J. Wilson, P. Gader, W. Lee, H. Frigui, and K. Ho, “A large-scale systematic evaluation of algorithms using ground-penetrating radar for landmine detection and discrimination,” *IEEE Transactions on Geoscience and Remote Sensing*, vol. 45, no. 8, pp. 2560–2572, 2007.
- ¹³ C. Ratto, P. Torrione, and L. Collins, “Exploiting ground-penetrating radar phenomenology in a context-dependent framework for landmine detection and discrimination,” *IEEE Transactions on Geoscience and Remote Sensing*, vol. 49, no. 5, pp. 1689–1700, 2011.
- ¹⁴ D. Sternlicht, J. Harbaugh, A. Shah, M. Webb, and R. Holtzapple, “Buried object classification using a sediment volume imaging sas and electromagnetic gradiometer,” in *Proceedings of IEEE OCEANS*, 2006, pp. 1–6.
- ¹⁵ R. Urick, *Principles of Underwater Sound*. McGraw-Hill, 1983.
- ¹⁶ D. Jackson and M. Richardson, *High-frequency seafloor acoustics*. Springer Science & Business Media, 2007.
- ¹⁷ R. Hansen, H. Callow, T. Sæbø, and S. Synnes, “Challenges in seafloor imaging and mapping with synthetic aperture sonar,” *IEEE Transactions on Geoscience and Remote Sensing*, vol. 49, no. 10, pp. 3677–3687, 2011.
- ¹⁸ Z. Lowe and D. Brown, “Multipath reverberation modeling for shallow water acoustics,” in *Proceedings of the 11th European Conference on Underwater Acoustics*, 2012, pp. 1285–1291.
- ¹⁹ D. Jackson, “APL-UW high-frequency ocean environmental acoustic models handbook,” *Applied Physics Laboratory, University of Washington, Technical Report*, vol. 9407, no. 102, pp. 1499–1510, 1994.
- ²⁰ H. Van Trees, *Detection, estimation, and modulation theory, part I: detection, estimation, and linear modulation theory*. John Wiley & Sons, 2004.
- ²¹ D. Williams, “The Mondrian detection algorithm for sonar imagery,” *IEEE Transactions on Geoscience and Remote Sensing*, vol. 56, no. 2, pp. 1091–1102, 2018.
- ²² G. Dobeck, J. Hyland, and L. Smedley, “Automated detection/classification of seamounts in sonar imagery,” in *Proceedings of the SPIE International Society of Optics*, vol. 3079, 1997, pp. 90–110.

- ²³ R. Fandos, A. Zoubir, and K. Siantidis, “Unified design of a feature based ADAC system for mine hunting using synthetic aperture sonar,” *IEEE Transactions on Geoscience and Remote Sensing*, vol. 52, no. 5, pp. 2413–2426, 2014.
- ²⁴ P. Viola and M. Jones, “Robust real-time object detection,” *International Journal of Computer Vision*, vol. 57, no. 2, pp. 137–154, 2004.
- ²⁵ G. Facciolo, N. Limare, and E. Meinhardt-Llopis, “Integral images for block matching,” *Image Processing On Line*, vol. 4, pp. 344–369, 2014.
- ²⁶ S. Kargl, K. Williams, T. Marston, J. Kennedy, and J. Lopes, “Acoustic response of unexploded ordnance (UXO) and cylindrical targets,” in *Proceedings of IEEE OCEANS*, 2010, pp. 1–5.
- ²⁷ Y. LeCun, Y. Bengio, and G. Hinton, “Deep learning,” *Nature*, vol. 521, no. 7553, p. 436, 2015.
- ²⁸ I. Gerg, “The advanced synthetic aperture sonar imaging engine (ASASIN), a time-domain backprojection beamformer using graphics processing units,” *The Journal of the Acoustical Society of America*, vol. 140, no. 4, pp. 3347–3347, 2016.
- ²⁹ J. Wallis and T. Miller, “Three-dimensional display in nuclear medicine and radiology,” *Journal of Nuclear Medicine*, vol. 32, no. 3, pp. 534–546, 1991.